Selective laser melting of high-strength primary AlSi9Cu3 alloy: Processability, microstructure, and mechanical properties

J. Fiocchi, C.A. Biffi *, A. Tuissi

CNR ICMATE, National Research Council, Institute of Condensed Matter Chemistry and Technologies for Energy, Unit of Lecco, CNR ICMATE, Via Previati 1/e, 23900 Lecco, Italy

HIGHLIGHTS

- AlSi9Cu3 alloy was produced by selective laser melting.
- Process optimization allowed to obtain fully dense samples, with a limited amount of defects.
- The high cooling speed induced a refinement of microstructure and influenced the precipitation processes.
- The mechanical properties of SLMed alloy are higher than the ones of the cast alloy.
- Heat treatment allowed to obtain a balanced set of mechanical properties thanks to microstructural modifications.

GRAPHICAL ABSTRACT
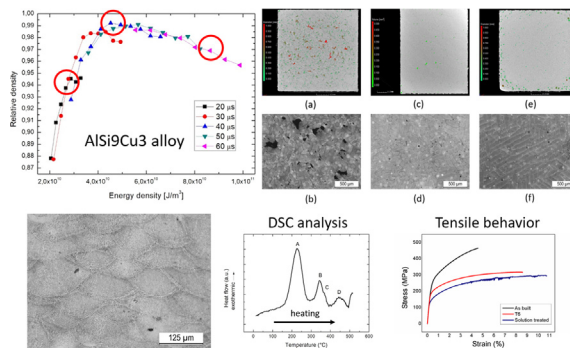
ARTICLE INFO

ABSTRACT

The present work explores the possibility of employing the selective laser melting technique to produce parts in AlSi9Cu3 alloy. This alloy, currently prepared by high-pressure dye casting and intended for automotive application, may benefit from the refined microstructure commonly induced by additive manufacturing techniques. The process parameters were systematically varied to achieve full density, and the resulting defects were studied. Thereafter, microstructural features were analyzed, revealing that the high cooling rate, induced by the process, caused a large supersaturation of the aluminum matrix and the refinement of the eutectic structure. Again, the precipitation of the reinforcing θ phase provided numerous nucleation sites. These features were found to be related to the mechanical behavior of the SLMed AlSi9Cu3 alloy, which outperformed the conventional casted alloy in terms of elongation to failure and strain hardening rate both in the as-built and heat treated conditions.

1. Introduction

In the last few decades, the use of aluminum alloys in the automotive industry has become of paramount importance in view of the need to reduce weight and thus obtain increased performances and reduced

* Corresponding author.
  E-mail address: carloalberto.biffi@cnr.it (C.A. Biffi).

fuel consumption. Among the used alloys, those based on the Al–Si–Cu system have attracted considerable interest owing to their widespread use in engine parts, in particular for thin-walled parts that are subjected to dynamic loading, such as cylinder heads [1]. The presence of silicon helps in reducing the melting temperature and in increasing the melt fluidity, thus making casting easier [2]. On the other hand, copper and possibly other alloying elements such as Mg improve the mechanical response of the material by solid solution and precipitation strengthening [3]. Among the alloys belonging to this system, the AlSi9Cu3 (wt%) alloy is a widely used one, usually processed by pressure die casting (PDC) or high-pressure die casting (HPDC) [4]. However, these production processes are known to possibly induce a number of defects, consisting of porosities, oxide layers, and blistering, which limit the possible applications of the produced parts [5,6]. In this respect, the possibility of employing different production techniques to synthesize the AlSi9Cu3 alloy looks extremely interesting. Selective laser melting (SLM), which belongs to a broad family of additive manufacturing (AM) technologies, has already found widespread use in both industrial and research fields and may be considered as a relatively mature technology [7–9]. In this light, the employment of SLM for manufacturing AlSi9Cu3 components may prevent some casting-induced defects and additionally provide several advantages, including greater design freedom, production flexibility, and integration of localized functionalities. Again, SLM induces an extremely fine microstructure, which positively affects the mechanical performances of the resulting product [10,11]. Fousova et al. [12] reported a successful attempt at producing AlSi9Cu3Fe alloy by SLM; they performed a deep microstructural analysis and compared the obtained results with the characteristics of the same alloy produced by HPDC. However, no optimization of the process parameters was reported, and, therefore, further studies appear to be necessary. Moreover, Pozdniakov et al. [13] synthesized a similar AlSi11CuMn alloy by SLM and obtained excellent strength but poor elongation to failure. Finally, Yamasaki et al. [14] studied the addition of different amounts of Fe to an AlSiCuMgNi alloy to improve its high-temperature mechanical properties.

The present experimental work provides further advancements in the knowledge of SLM of AlSi9Cu3 as a valid alternative to traditional processing methods and enables the production of three-dimensional light parts. In this light, a comprehensive technological approach has been implemented along with metallurgical correlations. First of all, the process parameters were varied to obtain optimal density and the resulting defects were studied. Defects analysis was performed by coupling density measurements, done by applying Archimedes's method, with computed tomography (CT), to guide the process optimization. Thereafter, the obtained SLMed alloy was analyzed microstructurally and its thermophysical behavior was studied kinetically, to understand and effectively exploit the precipitation of the reinforcing phases. Finally, the mechanical properties were evaluated and found to be more advance than those that could be obtained by conventional production methods. Moreover, a conventional thermal treatment, based on solution treatment and ageing (T6), was implemented in order to investigate the evolution of mechanical properties upon exposure to high temperatures and whether the development of dedicated thermal treatments is required.

2. Materials and experimental procedure

The primary AlSi9Cu3 (wt%) samples were produced from gas-atomized powder (supplied by LPW Technology, Ltd.), which exhibited the composition reported in Table 1, as determined by inductive coupled plasma (ICP) measurements. The powder, whose morphology is shown in Fig. 1a, had a size range of 20–63 μm. It should be noted that its shape is not perfectly rounded, displaying many satellites and irregularities, which may constitute a serious impedance to the acquisition of fully dense parts. The powder microstructure, resulting from the X-ray spectrum reported in Fig. 1b, is mainly composed of an α-Al

matrix (face-centered cubic, FCC) and of eutectic Si (FCC) and Al_2Cu (body-centered tetragonal) phases. The formation of the two eutectic phases was made possible by the relatively low cooling rate experienced by the powder particles during their production.

A Renishaw AM400 machine, based on a 400-W pulsed wave fiber laser and equipped with a reduced build volume, was used to produce different types of samples: small prisms for process optimization, rectangular bars for microstructural analysis, and 2-mm-thick laminas, lying in the sagittal plane, for tensile testing, as depicted in Fig. 1c. The schematics of the temporal and spatial distribution of the laser pulses are shown in Fig. 2a–b, respectively [15]. The use of different built samples was driven as function of the type of characterization; in fact, it is known that the geometry and size of the samples may affect the defects in SLM process [16,17].

In this work, laser power and exposure time were varied, according to the full design of the experiments, whereas the other process parameters were fixed, as listed in Table 2. The standard scanning strategy, namely, meander, was used to produce the samples (see Fig. 3): (i) the hatching was performed using a meander path, in which the investigated process parameters were changed, according to Table 2; (ii) the contour was performed with the standard indicators reported by the SLM producer. Each scanning layer was rotated by 67° with respect to the previous one, and the scheme was repeated every 180 layers.

Part density was measured by Archimedes's principle using a Gibertini E50S2 precision digital balance and considering a full density of 2.75 g/cm³, as reported in the technical datasheet of the powder. X-ray CT was performed on selected prisms using a Phoenix v|tome|x M 300 CT system (Baker Hughes) to highlight the types of defects within the entire volume of the samples.

Some of the samples built with optimized parameters were subjected to a conventional T6 treatment, based on solution treatment at 470 °C for 6 h, quenching and isothermal ageing at 160 °C for 24 h. Temperatures and durations of the performed treatments were chosen according to the results reported in [18].

Morphological analysis was carried out using an optical microscope (Leitz Aristomet) on both the xy and the xz sections to reveal the microstructure and defects of the samples. In-depth microstructural analyses were performed using an X-ray diffractometer (Panalytical X'Pert Pro using Cu Kα radiation operating at 40 kV and 30 mA on the xy surfaces of the samples in the 2theta range of 20°–120°) and a scanning electron microscope (SEM, mod. Leo 1413 operating at 20 kV). All microstructural observations were done on finely polished sections etched with Keller's reagent.

Thermal analyses were carried out by differential scanning calorimetry (DSC) using a Seiko DSC220C apparatus in a flowing nitrogen atmosphere. Continuous heating experiments were carried out at temperature ranges of 0 °C–550 °C at four heating rates of 5 °C/min, 10 °C/min, 15 °C/min, and 20 °C/min, respectively. The kinetics of the precipitation reactions were evaluated according to the Kissinger method and were double checked by the Friedman method, according to the procedures thoroughly described in the Supporting Material section [19–22].

Tensile tests were performed according to the E8/E8M-11 ASTM standard on sub-sized specimen with a crosshead speed of 0.5 mm/min (3.3 10^{-4} s^{-1}) using an MTS Alliance RT/100 universal testing machine at room temperature. At least three samples per condition were tested.

Table 1
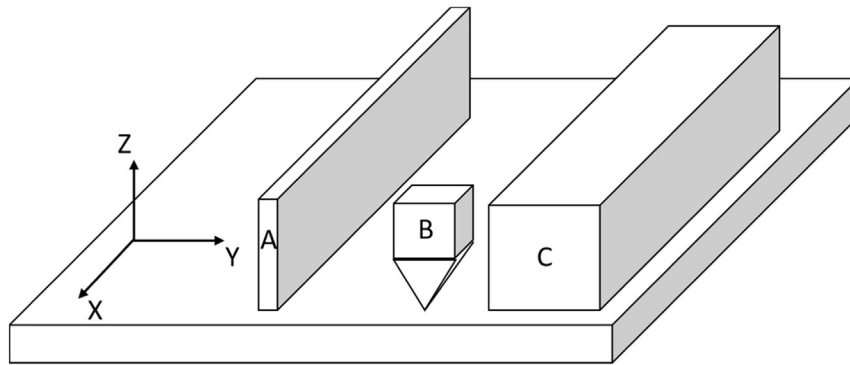Chemical composition of the utilized powder, as measured by ICP.

	Al	Si	Cu	Fe	Mg	Ti
Wt.%	Bal.	8,92	2367	0,339	0,028	0,007
Std dev.		0,625	0,106	0,001	0,009	0,0005
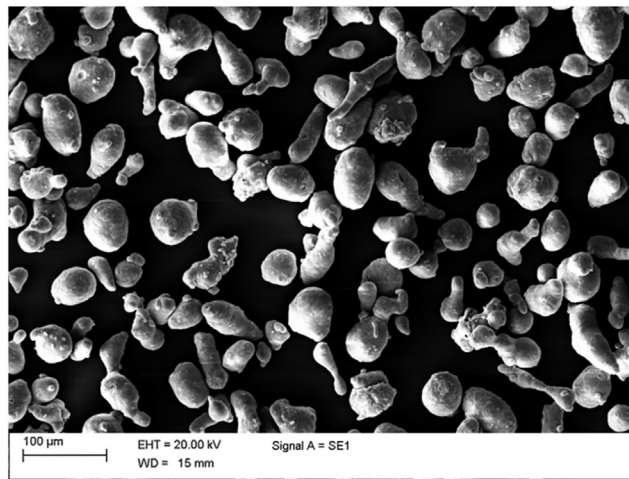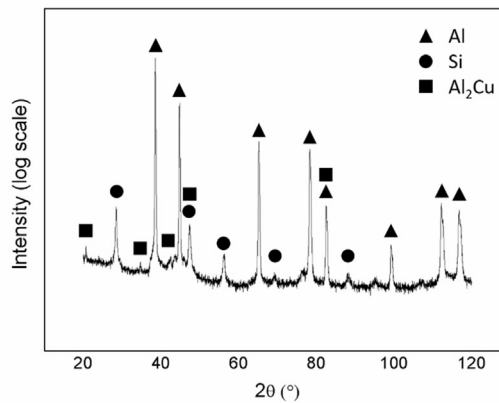
Fig. 1. SEM image (a) and XRD spectrum (b) of the AlSi9Cu3 powder; schematic of the built samples (c).

3. Results and discussion

3.1. SLM process optimization

The total energy transferred by the laser to the powder during processing may be described by a volumetric energy density (Ψ), whose expression for a pulsed wave laser in the absence of base-plate preheating is [10].

$$\Psi = \frac{P \cdot t_{ex_P}}{d_p \cdot d_h \cdot s} \tag{1}$$

where P is the laser power, t_{exp} is the exposure time, d is the point distance, s is the hatch spacing, and h is the layer thickness.

Identification of the feasibility window was performed by considering the main process parameters (power and exposure time), which are representative of the PW emission mode, aimed at the maximization of the relative density. Fig. 4 shows the effect of the energy density on the densification of the AlSi9Cu3 powder. In detail, the effect of exposure time is highlighted by different curves. Each curve represents the typical evolution of the Ψ on the relative density of a SLMed part: it is usual to observe a rapid increase in the relative density up to its maximum value and then a soft decrease with a limited slope for higher values of Ψ. From a qualitative point of view, this trend fits well the typical ones
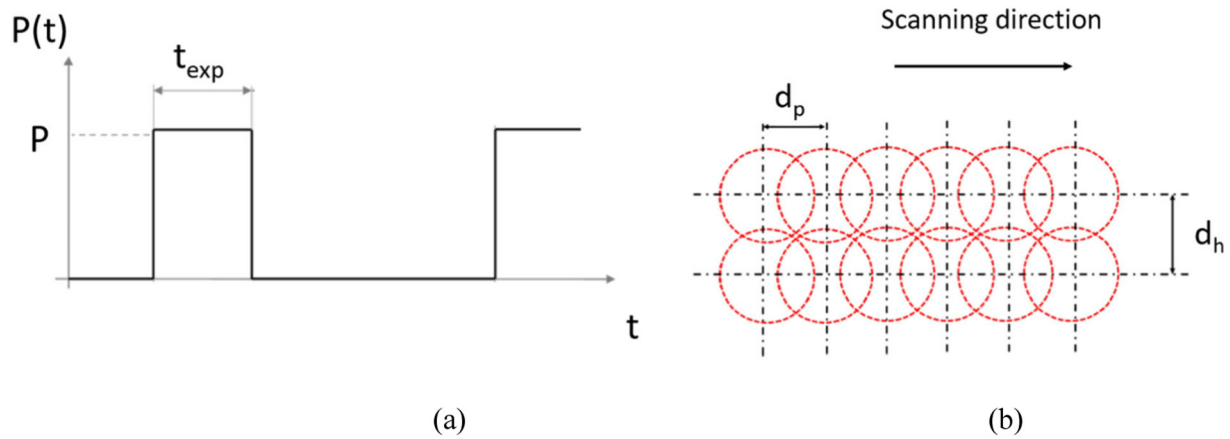
Fig. 2. Schematic of the temporal power profile and spatial pulses path (b) in SLM performed with PW emission mode [15].

revealed during the SLM process optimization for a variety of different materials [23]. The effect of exposure time on the relative density is a shift of the curve peak toward higher energy densities, as a function of the range of investigated values of Ψ (see Fig. 4).

In the case of the AlSi9Cu3 alloy, a steep increase in the relative density up to 99.2% was detected with increasing values of Ψ up to $45.3 \cdot 10^9$ J/m^3, which corresponds to the process condition ($P = 275$ W; $t_{exp} = 40$ μs). For higher energies, the relative density started to slowly decrease again.

This can usually be explained by considering that low-energy inputs cause defects, such as unmelted powders, due to lack of fusion, whereas high-energy ones induce porosity, correlated to gas entrapment and potential local vaporization of elements. The different nature of the defects, which can be located in different regions in the relative density evolution shown in Fig. 4, can be explained by the energy required by the material to allow its melting and its partial vaporization, according to the following equation:

$$E = A \cdot \rho \cdot \left\{ C_p \cdot [T_M - T_i] + L_M + m' \cdot L_V \right\} \tag{2}$$

where A is the absorption coefficient; r is the density; C_p is the thermal capacity; T_M and T_i are the melting and initial temperatures, respectively; L_M and L_V are the latent heat of melting and vaporization, respectively; and m' represents the percentage of liquid material that is subjected to vaporization, if present.

The system between Eqs. (1) and (2) represents the correlation between the volumetric energy density, which is characteristic of the defined process condition, and the energy required by the alloy for its melting and, eventually, for its partial evaporation ($m' > 0$). In the case of lack of fusion or formation of gas pores, Ψ would be lower or higher than E, respectively. This behavior is well confirmed by the results obtained by combining the CT scans and the metallurgical sections. In particular, three process conditions, fitting the investigated range of Ψ values, were analyzed. Fig. 5 show images of the entire xy view of the samples, obtained from CT, and its magnification, acquired with optical

microscopy (OM), respectively. Moreover, a quantitative analysis of the defects is reported in Fig. 6, where the characteristic diameter–sphericity trend is shown. Table 3 reports the process parameters used and the comparison of relative density values, measured via Archimedes's method and CT scans.

Fig. 5a confirms that a large number of defects are present, mainly located in the central part of the sample, that significantly reduce the relative density to below 97%. The mechanism of defect formation is associated with the lack of complete fusion due to the insufficient energy ($\Psi = 28.8 \cdot 10^9$ J/m^3) provided by the laser scan to the AlSi9Cu3 powder, as confirmed by the OM image in Fig. 5b. In Fig. 6a, a quadratic trend of the diameter–sphericity ratio of the detected defects can be seen. In detail, in the first area of the plot (indicated as Region 1), large defects, in the range 0.3–2 mm, are characterized by a low sphericity. These elongated and irregular voids are associated with the lack of fusion oriented along a preferential direction, related to the laser scanning. A limited percentage of the detected defects have a small size, up to 0.4 mm, and their shape is more circular, located in Region 2. This type of defect is due to the incomplete fill of the liquid material in the space among adjacent powders.

With increasing energy density, the powder receives more energy for the formation of a more uniform and stable liquid pool, which allows
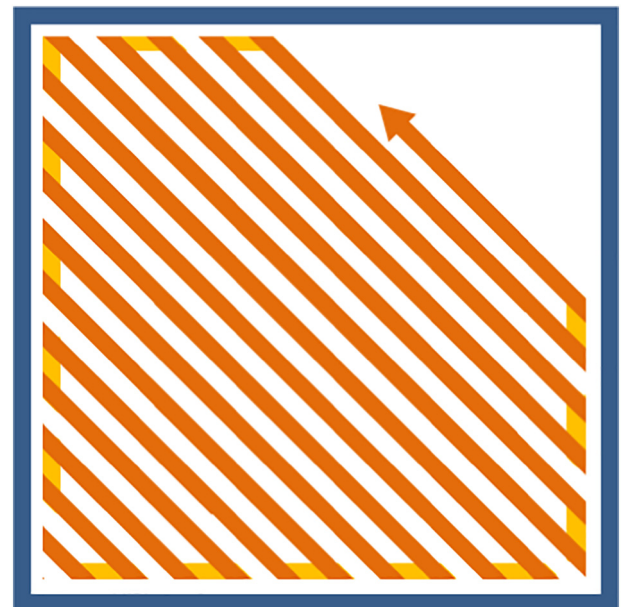
Table 2
Varied and fixed process parameters.

Varied parameters	Power [W]	175-200-225-250-275 300-325-350-375-400
	Exposure time [μs]	20–30–40–50–60
Fixed parameters	Hatch distance [μm]	90
	Point distance [μm]	90
	Laser spot size [μm]	65
	Atmosphere	Ar
	Thickness layer [μm]	30
	Platform temperature [°C]	30

Fig. 3. Scanning strategy, namely meander, used during the SLM experiments.
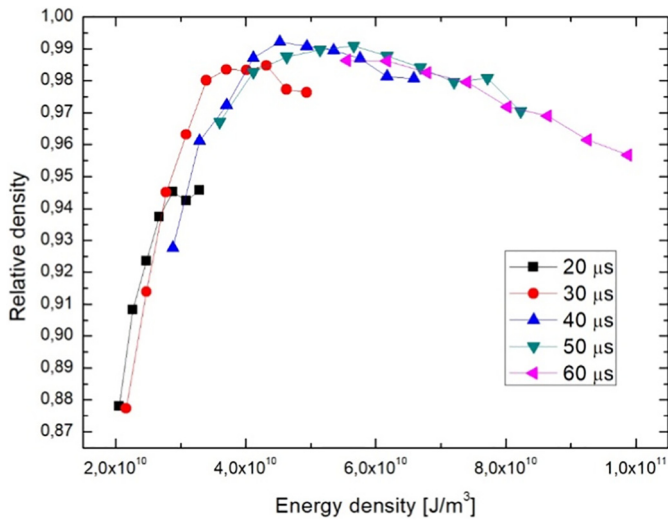
Fig. 4. Evolution of the relative density as function of energy density Ψ.

for an increase in the relative density of the SLMed part. At $\Psi = 45.3 \cdot 10^9$ J/m^3, corresponding to the peak indicated by the curve in Fig. 4, few and small-sized pores can be detected by CT scan (Fig. 5c) and confirmed by the OM micrograph: only spherical pores can be observed. Fig. 6b indicates that smaller defects with an almost spherical shape are generated. The area in the plot of Fig. 6b is overlapped in Region 2 with the defects generated with a low Ψ value. It can be expected that the pores characteristic of Region 2 should be the least dangerous among the geometrical defects, as their limited dimensions and high sphericity could reduce the stress concentrations in terms of fatigue

issues. However, the size and shape are equivalent and, therefore, they are associated with the same mechanism of defect formation. According to these different defect distributions, CT analysis allowed to determine an increase in the relative density from 96.7% up to 99.9% (see Table 3).

With the further increase in Ψ up to $92.6 \cdot 10^9$ J/m^3, the liquid pools become less stable and potential evaporation of elements having a low boiling point can occur. Moreover, gas entrapment within the liquid pool during its solidification can lead to the formation of spherical pores. In this case, CT scan indicates that the porosity is located mainly in proximity to the sample border (see Fig. 5e), whereas the central part looks almost fully dense (around 98%). As depicted in Fig. 6c, the shape of these pores looks spherical as the pores were generated with $\Psi = 45.3 \cdot 10^9$ J/m^3, although their size increased, probably because of the larger amount of material that vaporized during the SLM process and because of the higher shielding gas entrapment during the solidification of the liquid pool.

3.2. Compositional and microstructural characterizations

The composition of the as-built samples was determined by ICP measurements and is reported in Table 4. An overall reduction in the amounts of alloying elements with respect to those measured in the fresh powder is apparent. This decrease heavily affected the trace elements, making their abundance practically negligible. The alloy can thus be rightfully considered as a primary AlSiCu one. The X-ray spectrum reported in Fig. 7 is mainly characterized by α-Al and eutectic Si peaks. Moreover, it also shows the presence of a the Al$_2$Cu phase, whose amount seems anyway smaller than the one revealed in fresh powder. Even under high cooling rates typical of the SLM process, the formation of a limited amount of Al$_2$Cu secondary phase was allowed. Its dimensions are likely limited, since no such phase could be found during SEM inspection of the considered samples. Their presence is
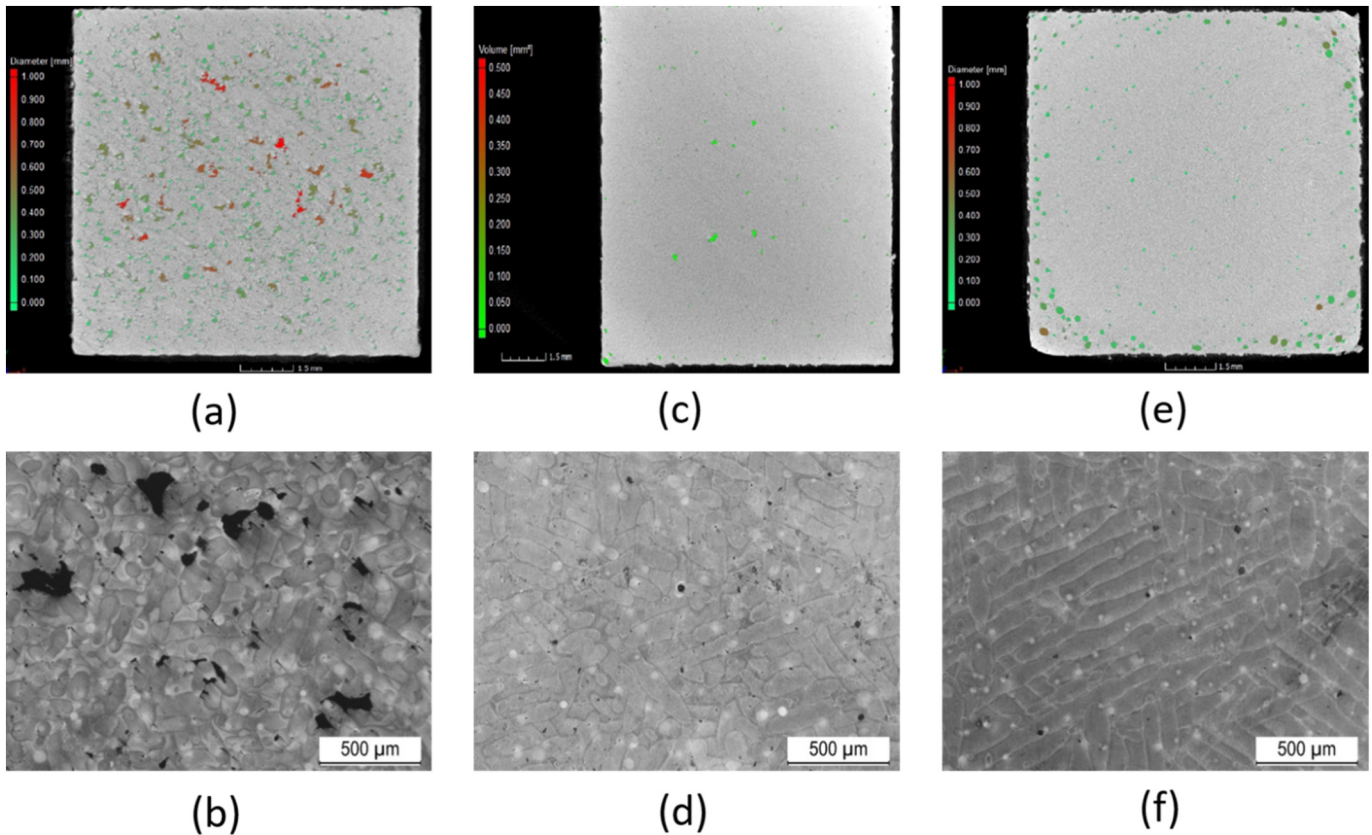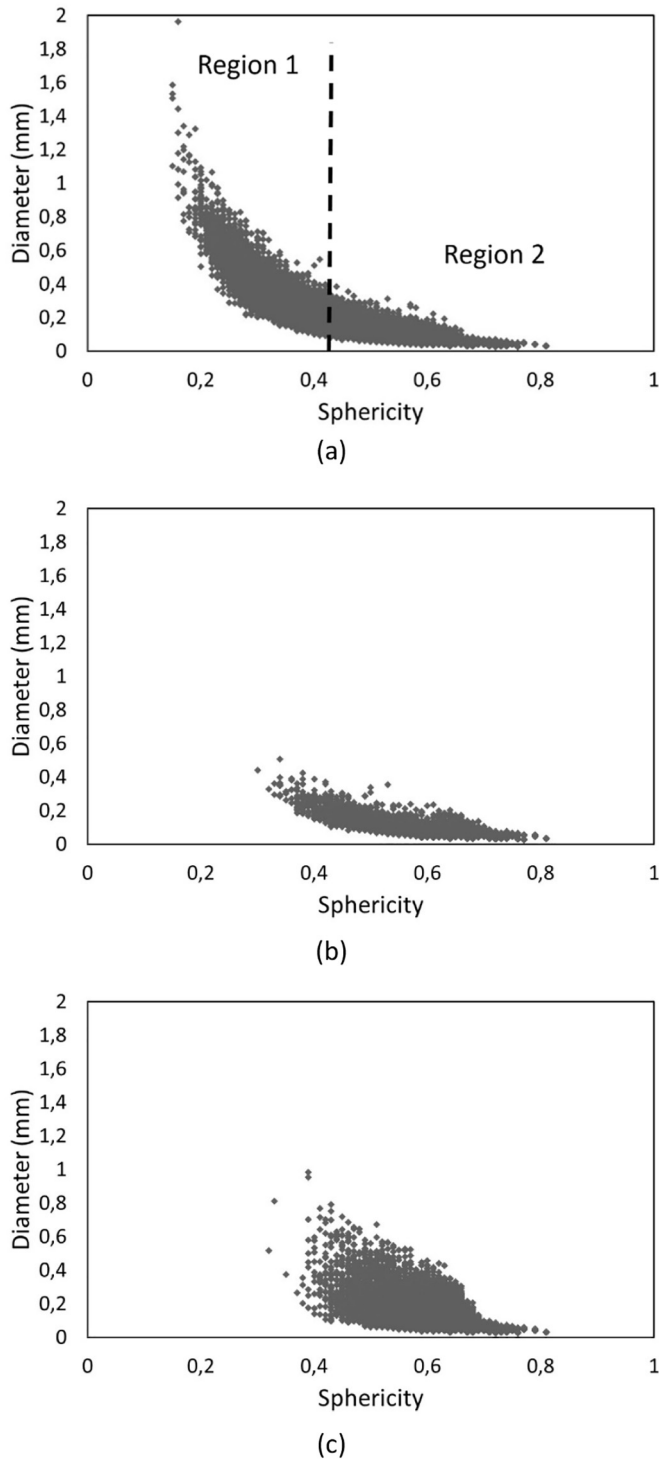

Fig. 5. Analysis of defects, by CT and OM respectively, of samples manufactured with different energy density values: $\Psi = 28.8 \cdot 10^9$ J/m^3 (a–b); $\Psi = 45.3 \cdot 10^9$ J/m^3 (c–d) and $\Psi = 92.6 \cdot 10^9$ J/m^3 (e–f).

(a)

(b)

(c)

Fig. 6. Diameter-sphericity trend measured through CT scans of built samples manufactured with different energy density values: $\Psi = 28.8 \cdot 10^9$ J/m^3 (a–b); $\Psi = 45.3 \cdot 10^9$ J/m^3 (c–d) and $\Psi = 92.6 \cdot 10^9$ J/m^3 (e–f).

Table 4

Chemical composition of the as built samples, as measured by ICP.

	Al	Si	Cu	Fe	Mg	Ti
Wt.%	Bal.	7291	2317	0,065	0,003	0,009
Std dev.		0,175	0,129	0,001	0,002	0,001

however confirmed by the results reported by Fousova et al. [12], who recognized the presence of particles with Al$_2$Cu composition thanks to EDS analysis coupled to TEM observations.

Optical micrographs of the as-built samples, along both the xy and the xz planes, are reported in Fig. 8a and b, respectively. As typical of SLM-built parts, the samples are composed of superimposed melt pools, which appear as elongated bands in the xy plane and as semi-circular in the xz one (parallel to the building direction). The dimensions of the melt pools (113.2 $\pm$ 8.2 μm in width; 31.9 $\pm$ 6.7 μm in height) appear to be consistent with the processing parameters used (see Section 2) and with the previous results on other Al-Si alloys processed by the same SLM apparatus [10]. At higher magnification (Fig. 8c and d), the cellular aluminum–silicon eutectic structure is evident, comprising a supersaturated α-Al matrix and an almost continuous Si-rich network. As a consequence of the overlapping of successive laser scans, an alternation of fine fusion zones and coarse heat-affected zones arises. The average dimension of the network cell in the fine fusion zone in the xy plane was evaluated by the Heyn linear intercept method (ASTM E112), and the result was 658 $\pm$ 26 nm, which is slightly larger than the value reported in [24] for a SLMed AlSi10Mg alloy produced by a similar Renishaw AM250 apparatus.

In Fig. 9, the DSC curve of the as-built sample, recorded at 10 °C/min, is reported and the revealed exothermic phase transformation peaks are marked by capital letters (A, B, C, and D). According to previous literature results on similar alloys, peak A is attributed to the precipitation of θ″ [25], peak B to the formation of θ′, peak C to the rupture and spheroidization of the Si network [26], and peak D to the appearance of the θ phase. It is known from literature studies that the AlSi9Cu3 alloy is usually characterized by the coexistence of three precipitation sequences, namely, the θ-Al$_2$Cu, β-Mg$_2$Si, and Q-Al$_5$Mg$_8$Cu$_2$Si$_6$ ones [4]. However, the exothermic effects revealed by DSC in the present work, apart from peak C, may be reasonably attributed to the θ sequence only because of the extremely low Mg content revealed by ICP measurements. This Mg depletion is believed to have hindered the formation of the β and Q phases. The peak temperatures and formation enthalpies of the exothermic phenomena A, B, C, and D are reported in Tables 5 and 6, respectively.

To evaluate the kinetics of the precipitation phenomena, we analyzed DSC curves registered at different heating rates using the Kissinger isoconversional method, as reported in the Supporting Materials Section. Table 7 reports the activation energy and frequency factor values calculated for the θ″, θ′, and θ precipitation, as well as for the Si dissolution and Si network rupture and spheroidization. To verify the reliability of the performed evaluations, we computed activation energies using the Friedman method, which yielded the following results: 128.1 kJ/mol for θ″, 241.6 kJ/mol for θ′, 182.7 kJ/mol for the Si-related process, and 238.0 kJ/mol for the θ precipitation. It should be noted that, for all the considered transformations, the two computing methods yielded similar values, thus allowing reasonable confidence in the obtained results. In the following, the kinetics of the θ precipitation sequence will

Table 3

Comparison between the density values obtained through Archimedes's method and through CT analysis.

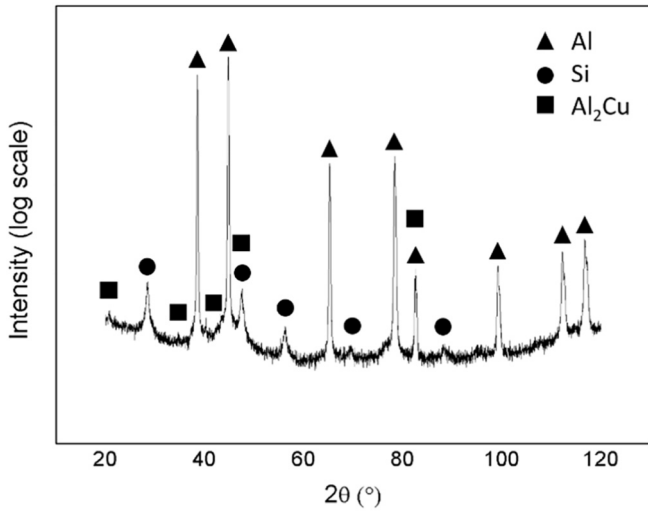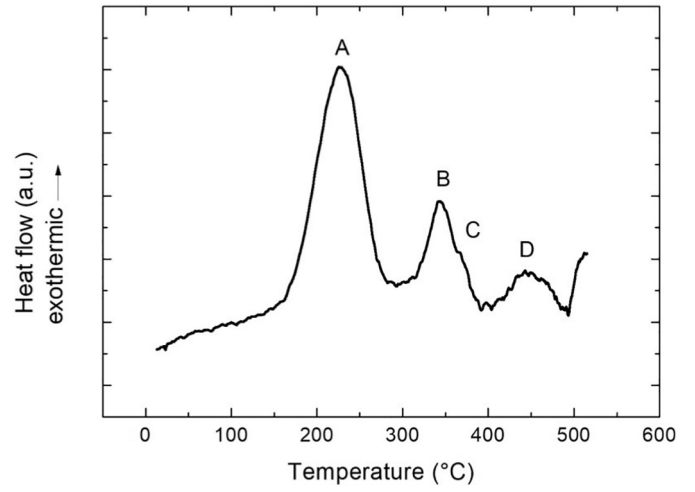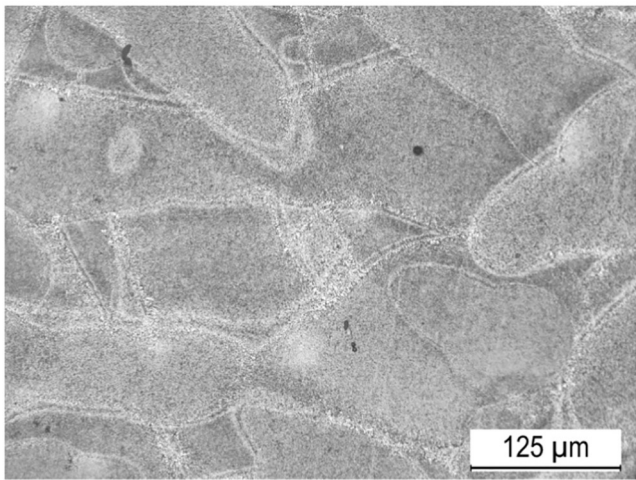| Power [W]	Exposure time [μs]	Ψ [J/m^3]	Archimedes density [%]	CT density [%]
350	20	$28,8 \cdot 10^9$	94.52	96.73
275	40	$45,3 \cdot 10^9$	99.23	99.87
375	60	$92,6 \cdot 10^9$	96.16	97.94

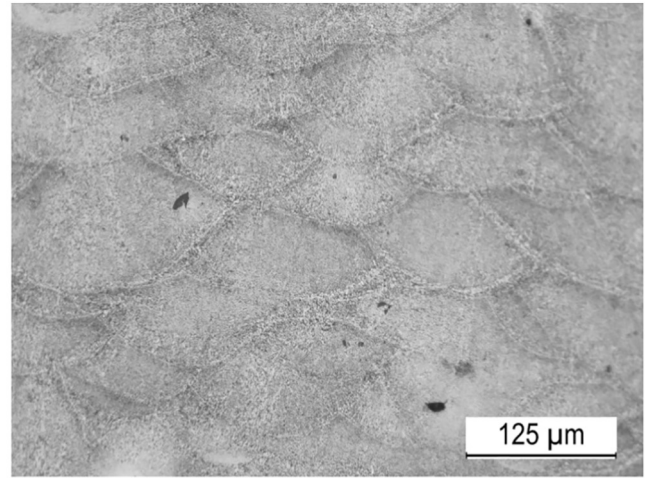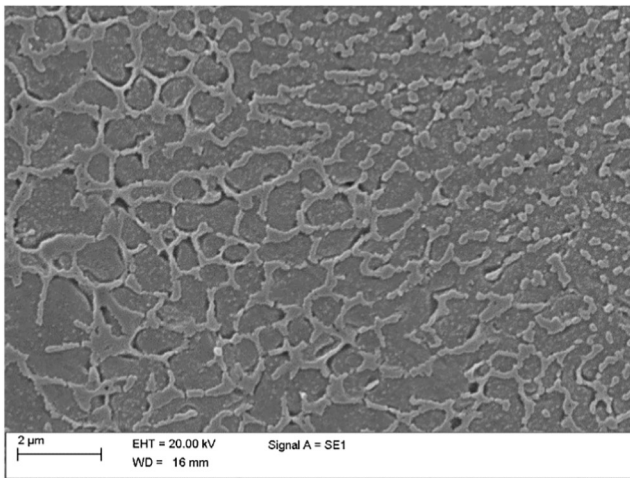Fig. 7. XRD spectrum of as-built AlSi9Cu3 alloy.

Fig. 9. DSC curve of the as-built AlSi9Cu3 alloy recorded at 10 °C/min.
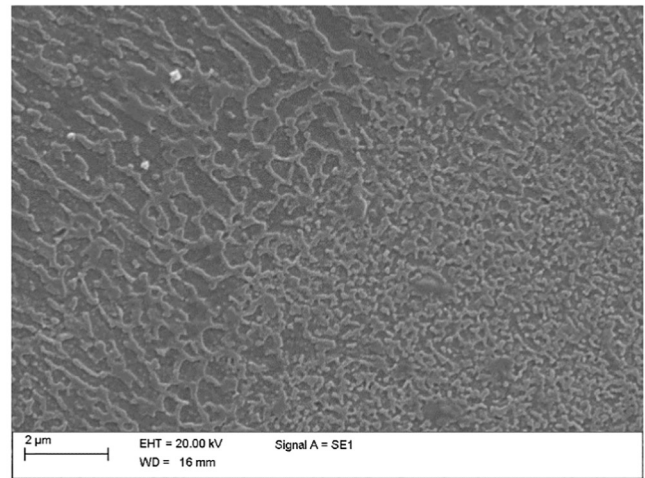

(a)

(b)

(c)

(d)

Fig. 8. Optical and SEM micrographs of as-built AlSi9Cu3 alloy along xy (a,c) and xz (b,d) planes, respectively.

Table 5
Peak temperatures of exothermic transformations A, B, C and D, as shown in Fig. 9.

Heating rate (°C/min)	Peak temperature (°C)			
	Peak A (θ″)	Peak B (θ′)	Peak C (Si)	Peak D (θ)
5	220,2	339,2	–	438,9
10	225,3	344,9	371,4	443,0
15	241,2	351,5	379,4	450,4
20	245,5	356,7	384,3	456,1

Table 7
Kinetic parameters relative to exothermic phenomena, as computed by Kissinger's method.

	Peak A (θ″)	Peak B (θ′)	Peak C (Si)	Peak D (θ)
Activation energy (KJ/mol)	102,9	237,8	177,3	224,1
Frequency factor (s^{-1})	$4,03 \times 10^8$	$1,35 \times 10^{18}$	$1,97 \times 10^{12}$	$1,81 \times 10^{14}$

be discussed first, followed by the analysis of the results regarding Si spheroidization.

θ″ precipitation is characterized by an activation energy (115.5 kJ/mol on average) that is very similar to the values reported in [26–28] and slightly smaller than that computed by Rylands et al. [29]. The obtained activation energy value is a little lower than the values reported in the literature for the diffusion of Cu in Al (140 kJ/mol [29], 141 kJ/mol [30], and 137 kJ/mol [31]), thus reasonably indicating that the phenomenon is based on the bulk diffusion of Cu atoms across the aluminum matrix. θ″ precipitates are known to usually evolve from previously formed Guigier-Preston (GP) zones: the relatively low measured activation energy thus suggests that GP zones are already present in the as-built samples, probably because of the heating cycles that occur during the building process, and act as favorable nucleation sites for θ″ precipitates. This observation is confirmed by the absence of the GP zone-related peak in the DSC scan in Fig. 9. Moreover, as reported in [32], a further reduction in activation energy with respect to that of the Cu diffusion may be ascribed to external stresses, which are present in SLM-built parts as solidification-induced residual stresses [33]. On the other hand, the θ′ precipitation process is characterized by an activation energy (237.8 kJ/mol according to the Kissinger method) that is evidently higher than that characterizing θ″ in the present work. In [34], θ′ is characterized by a much lower activation energy (between 66 kJ/mol and 77 kJ/mol). Because θ′ preferentially nucleates heterogeneously on dislocations [35,36], its high activation energy in the SLM-built samples may indicate that a small number of dislocations are available. This seems to be a reasonable conclusion for a fusion-based synthesis method, even though some studies [37,38] have shown that dense dislocation networks build up in nickel-based alloys and steels during the SLM process. However, to the best of the authors' knowledge, no such observation has been done as far as undeformed SLMed aluminum alloys are concerned [39]. θ precipitation is driven by a measured activation energy of 224.1 kJ/mol, which lies at the low end of the range reported by Elgallad et al. [34] for θ formation in a water-quenched AA2219 alloy (200–360 kJ/mol) and is lower than that reported in [28]. This process exhibits two possible formation mechanisms, which have been described in the literature: nucleation at the interface of grown θ′ precipitates and direct formation from the supersaturated α-Al matrix. This latter mechanism has also been shown to frequently occur at grain boundaries. In this view, it seems reasonable that the fine-grained structure resulting from the SLM process [8,10] makes θ formation easier by providing a great number of possible sites for heterogeneous nucleation. Finally, the rupture and spheroidization of the Si network process exhibited an average activation energy of 177.3 kJ/mol, according to the Kissinger method, which is slightly higher than that previously computed by the authors for the same phenomenon in an AlSi10Mg alloy [24,40]. Moreover, this value optimally fits the activation energy for bulk interdiffusion of Si in Al [41] and for the dissolution of Si precipitates in an Al matrix [42].

The frequency factors K_0, also called pre-exponential factors, are also reported in Table 7. This parameter describes the probability that an atom that has reached the necessary activation energy joins the growing precipitate nucleus [43] and is thus related to the availability of atoms to be involved in the considered transformation. The value obtained for the θ″ formation is close to that reported in [28] for the formation of GP zones, which are similar in structure to that of θ″ itself. This may indicate that the high supersaturation of the α-Al matrix provides a large reservoir of Cu atoms for the precipitation process. On the contrary, θ′ formation appears to occur at a much higher frequency in the SLM-built material than that in the conventionally produced ones. Nevertheless, the effect of K_0 on precipitation is likely to be superseded by the large energy barrier to be overcome, as reported earlier. Finally, θ formation occurs at quite a slow pace, thus indicating that overaging processes might require long exposures at elevated temperatures to be triggered. A reasonable preservation of the constant mechanical performances of the present material during prolonged high-temperature service may thus be expected.
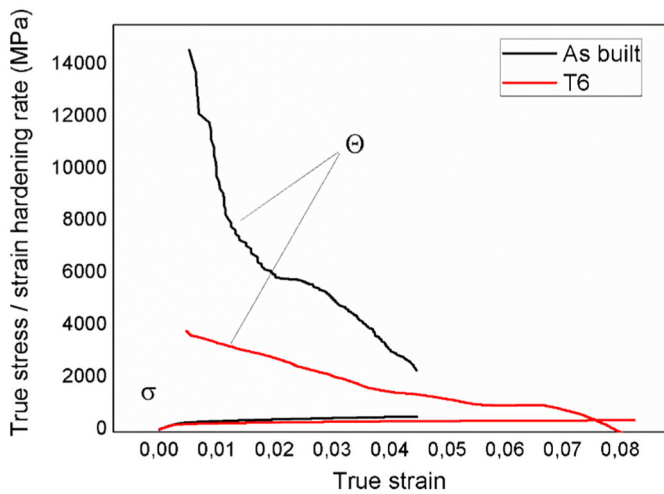
3.3. Mechanical characterization of the SLM-built material

The uniaxial tensile response of the SLMed AlSi9Cu3 alloy in as-built, solution treated and T6 condition is reported in Fig. 10a. It is worth noting that the alloy in the as-built condition exhibits a typical elasto-plastic behavior. After yielding, the curve is characterized by an elevated strain hardening rate, which has been ascribed to the silicon supersaturated solid solution induced by rapid solidification [44]. The mechanical behavior of the similar EN AC-46000 alloy has been widely studied and is also normed by EN standards: the standard values and literature results of the yield stress (YS), ultimate tensile stress (UTS), and elongation to failure (EF) are reported in Table 8. It is evident that the SLM-built parts outperformed the samples produced by conventional production methods. This is true both for the stress values, which were increased by the multiple strengthening mechanisms that act in additively manufactured aluminum alloys [45,46], and for the EF, whose high value was a result of the small number of defects present in the samples, as confirmed by CT analyses (see Section 3.1). Moreover, a comparison was made with the results reported by Fousova et al. [12] and by SLM Solutions datasheet [47] for a SLM-built AlSi9Cu3 alloy. The values obtained under the same conditions in the two cited works were largely higher in both strength and elongation fields. This may be due to the higher relative density and the smaller number of defects in the samples considered in the present study. In fact, even though the authors declared a residual porosity as low as 0.5%, no optimization of the process parameters is described in [12] and quite a relevant amount of porosity is evident in the SEM image of the fractured sample. The solution treatment induced a general decrease of strength, reducing both yield stress, now reading 152,5 MPa, and ultimate tensile strength, which was lowered down to 300,1 MPa. On the other hand, elongation to failure was drastically improved, reaching a satisfactory 11%. It shall be noted that these values are still higher than the ones required by

Table 6
Phase formation enthalpies related to exothermic phenomena, measured during a DSC scan performed at 10 °C/min.

	Peak A (θ″)	Peak B (θ′)	Peak C (Si)	Peak D (θ)
Enthalpies of phase formation (J/g)	26,4	5,8	0,9	3,2
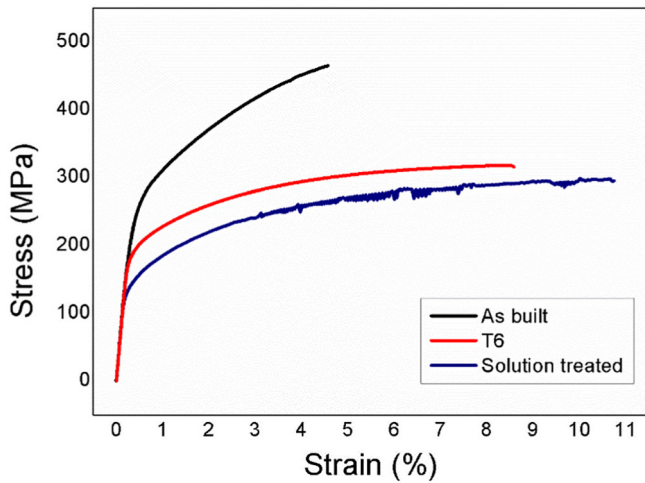
Fig. 10. (a) Engineering stress-strain curve of as-built, solution treated and aged (T6) and (b) true stress-strain curve, σ, and strain hardening rate, Θ, of as-built and solution treated and aged (T6) AlSi9Cu3 samples under tensile conditions.
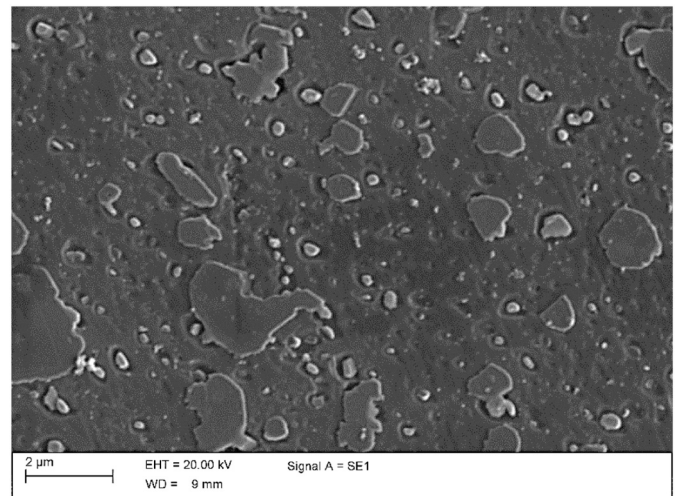
EN standards for the present alloy (Table 8). Moreover serrated plastic flow, which is connected on a microscopic level to dynamic strain ageing (DSA), characterizes the plastic deformation of solution treated samples. This phenomenon is related to the interaction of moving dislocations with clouds of diffusing solute atoms. The subsequent ageing treatment (T6) allowed an increase of strength through precipitation hardening (YS = 206 MPa, UTS = 318,7 MPa), while a satisfactory elongation to failure of 7,8% was still kept. Nevertheless, the initial strength

Table 8
Mechanical properties of AlSi9Cu3 alloy obtained by casting or selective laser melting.

		YS (MPa)	UTS (MPa)	Elongation (%)
CAST	EN 1706:1998 standard	140	240	1%
	Fousova et al. [12]	173 ± 14	257 ± 17	1.2 ± 0.5
	Dobrzañski et al. [53]	–	267	–
	Panušková et al. [54]	–	210	–
	Sanna et al. [4]	160	270	2.5
	Zamani et al. [55]	155	320	4.5
	Voncina et al. [56]	196	252	2.9
SLM	Fousova et al. [12]	219 ± 20	374 ± 11	1.9 ± 0.2
	SLM solutions datasheet [47]	236 ± 8	415 ± 15	5.0 ± 2.0
	Present work	266.1 ± 0.1	462.5 ± 3.0	4.5 ± 0.1

of the as-built sample could not be reached. Moreover, the formation of precipitates likely reduced the number of free solute atoms, thus hindering the formation of stress serrations. The lowering of strength with respect to the as-built samples might be ascribed to a number of causes, including the removal of residual stresses [33,48–50], change of morphology of the Si network [24] and an overall reduction of the supersaturation characterizing the initial solid solution. Some of these assumptions could be confirmed by analyzing SEM micrographs of the T6-treated alloy, as shown in Fig. 11. Coarse eutectic Si particles, whose dimensions approximately range from 3 μm to 0,5 μm, were formed as a result of the rupture of the original Si network and the subsequent coarsening during holding at high temperature. Beside these phases, the formation of numerous smaller Cu-rich precipitates (as revealed by EDS analysis) was induced. These precipitates, which may be reasonably recognized as θ phases, were formed during solution treatment: this may have limited the amount of Cu atoms available for precipitation during ageing, thus reducing the effectiveness of ageing treatment. Moreover, since they are coarse and incoherent with respect to the matrix, their effectiveness in strengthening the alloy is believed to be rather limited.

Compared with the widely available SLMed AlSi10Mg alloy [33,45,51], in the as-built state, the AlSi9Cu3 alloy is characterized, on average, by a lower YS and a higher UTS. This discrepancy suggests that higher strain hardening occurred in the alloy under investigation. To confirm this hypothesis and better describe the mechanical behavior of the SLMed alloy, the strain hardening rate Θ was computed as the derivative of the true stress against the true strain ($\Theta = \frac{d\sigma}{d\varepsilon}$). The resulting evolution of Θ is depicted in Fig. 10b for both the as-built and the T6 samples. As far as the as-built condition is concerned, the strain hardening rate appears to be extremely high for low plastic elongations (14,500 MPa), and then it decreases to a still large value of about 2300 MPa at the break point. The large Θ values have been explained in the literature [45] as being related to the formation of a greater number of Orowan loops around the nanometric Si precipitates dispersed across the aluminum matrix in AlSiMg alloys. In the present case, this effect may likely be enhanced by the presence of fine Cu-containing GP zones, as discussed in Section 3.2, which act as further pinning points for dislocation glide. This strengthening contribution may explain why the Θ values are higher than those described by Chen et al. [45]. Finally, as confirmed by previous literature results [45,52], the SLMed alloy did not reach a condition that satisfied Considère's criterion (i.e., the Θ and σ curves did not intersect each other). This means that a uniform elongation was not achieved and that failure occurred before necking because of structural defects. On the contrary, the solution treated and

Fig. 11. SEM micrograph of T6-treated AlSi9Cu3 alloy.

aged material was able to meet Considère's criterion at a true strain of 0,078, which is in good agreement with the value (0,081) corresponding to the measured UTS. This result may indicate that the profound microstructural transformation induced by the T6 treatment made the material able to reach a uniform elongation condition and withstand its inherent defects. Much reduced Θ values, which are lower than 4000 MPa all over the entire deformation range, may be ascribed to the reduced effectiveness in dislocation locking of coarsened Si and Cu-bearing precipitates and to the lower supersaturation of the solid solution. The measured strain hardening values closely match the ones reported in [45] for the AlSi10Mg alloy produced by powder metallurgy, further confirming that the T6 treatment gave rise to a microstructure which, although fine, more closely resembles the one obtainable through conventional processing routes.

4. Conclusions

The present study investigated the processability and the corresponding microstructural and mechanical properties of a new Al alloy composition, namely, AlSi9Cu3, by using selective laser melting (SLM) in the as-built condition. In detail, the principal results can be highlighted as follows:

- Fully dense samples (relative density of 99.9% measured by computed tomography) were manufactured through optimization of the main process parameters, i.e., laser power and exposure time. The defect sizes and shapes were also analyzed as a function of the energy density, by determining a region characterized by a limited size and an almost spherical shape.
- The microstructure was strongly refined by the high cooling rate induced by SLM, yielding a eutectic Al-Si structure similar to that of the widely available AlSi10Mg alloy. The resulting matrix supersaturation and crystal defects were shown to affect the precipitation behavior of the alloy from a kinetic point of view. A redefinition of proper heat treatments thus appears to be desirable in view of fully exploiting the alloy potential.
- The mechanical properties of the SLM-built AlSi9Cu3 alloy constitute a vast improvement over those shown by both conventionally produced parts and previous literature results in both strength and ductility. The high strain hardening capability, typically induced by Si nanoprecipitates in SLMed Al-Si alloys, is further improved in the present alloy by the presence of GP zones. A conventional T6 treatment was found able to strongly improve the material's ductility, even if it decreased strength.

Credit author statement

All the authors contributed to the manuscript preparation.
Fiocchi performed the characterizations, Biffi worked on the 3D printing process and Tuissi focused the main goals of the work.

Declaration of competing interest

The authors confirm that there are no known conflicts of interest associated with this publication.

Acknowledgments

Data availability

The raw/processed data required to reproduce these findings cannot be shared at this time as the data also form part of an ongoing study.

Appendix A. Supplementary data

Supplementary data to this article can be found online at https://doi.org/10.1016/j.matdes.2020.108581.

References

[1] H. Ye, An overview of the development of Al-Si-alloy based material for engine applications, J. Mater. Eng. Perform. 12 (2003) 288–297.
[2] I.J. Polmear, Light Alloys: Metallurgy of the Light Metals, John Wiley & Sons Australia, 1995.
[3] S.P. Ringer, T. Sakurai, I.J. Polmear, Origins of hardening in aged Al-Cu-Mg-(Ag) alloys, Acta Mater. 45 (1997) 3731–3744, https://doi.org/10.1016/S1359-6454(97)00039-6.
[4] F. Sanna, A. Fabrizi, S. Ferraro, G. Timelli, P. Ferro, F. Bonollo, Multiscale characterisation of AlSi9Cu3 (Fe) die casting alloys after Cu, Mg, Zn and Sr addition, Metall. Ital. 4 (2013) 13–24.
[5] Z. Ma, A.M. Samuel, F.H. Samuel, H.W. Doty, S. Valtierra, A study of tensile properties in Al-Si-Cu and Al-Si-Mg alloys: effect of β-iron intermetallics and porosity, Mater. Sci. Eng. A 490 (2008) 36–51, https://doi.org/10.1016/j.msea.2008.01.028.
[6] G. Timelli, A. Fabrizi, The effects of microstructure heterogeneities and casting defects on the mechanical properties of high-pressure die-cast AlSi9Cu3(Fe) alloys, Metall. Mater. Trans. A. 45 (2014) 5486–5498, https://doi.org/10.1007/s11661-014-2515-7.
[7] C.A. Biffi, A. Tuissi, Stato dell'arte sulle tecniche di produzione additiva per metalli, Metall. Ital. 1 (2017) 5–10.
[8] J. Zhang, B. Song, Q. Wei, D. Bourell, Y. Shi, A review of selective laser melting of aluminum alloys: processing, microstructure, property and developing trends, J. Mater. Sci. Technol. 35 (2019) 270–284, https://doi.org/10.1016/j.jmst.2018.09.004.
[9] T. Yu, H. Hyer, Y. Sohn, Y. Bai, D. Wu, Structure-property relationship in high strength and lightweight AlSi10Mg microlattices fabricated by selective laser melting, Mater. Des. 182 (2019), 108062. https://doi.org/10.1016/j.matdes.2019.108062.
[10] C.A. Biffi, J. Fiocchi, P. Bassani, A. Tuissi, Continuous wave vs pulsed wave laser emission in selective laser melting of AlSi10Mg parts with industrial optimized process parameters: microstructure and mechanical behaviour, Addit. Manuf. 24 (2018) 639–646, https://doi.org/10.1016/j.addma.2018.10.021.
[11] Q. Jia, P. Rometsch, S. Cao, K. Zhang, X. Wu, Towards a high strength aluminium alloy development methodology for selective laser melting, Mater. Des. 174 (2019), 107775. https://doi.org/10.1016/j.matdes.2019.107775.
[12] M. Fousova, D. Dvorsky, M. Vronka, D. Vojtech, P. Lejcek, The use of selective laser melting to increase the performance of AlSi9Cu3Fe alloy, Materials (Basel) 11 (2018) 1918, https://doi.org/10.3390/ma11101918.
[13] A.V. Pozdniakov, A.Y. Churyumov, I.S. Loginova, D.K. Daubarayte, D.K. Ryabov, V.A. Korolev, Microstructure and properties of novel AlSi11CuMn alloy manufactured by selective laser melting, Mater. Lett. 225 (2018) 33–36, https://doi.org/10.1016/j.matlet.2018.04.077.
[14] S. Yamasaki, T. Okuhira, M. Mitsuhara, H. Nakashima, Effect of Fe addition on heat-resistant aluminum alloys produced by selective laser melting, Metals (Basel) 9 (2019) 1–9, https://doi.org/10.3390/met9040468.
[15] A.G. Demir, P. Colombo, B. Previtali, From pulsed to continuous wave emission in SLM with contemporary fiber laser sources: effect of temporal and spatial pulse overlap in part quality, Int. J. Adv. Manuf. Technol. (2017) 1–14, https://doi.org/10.1007/s00170-016-9948-7.
[16] M.C.H. Karg, B. Ahuja, S. Wiesenmayer, S. Vyacheslavovich Kuryntsev, M. Schmidt, Effects of process conditions on the mechanical behavior of Aluminium wrought alloy EN AW-2219 (AlCu6Mn) additively manufactured by laser beam melting in powder bed, Micromachines (2017) 8, 23, https://doi.org/10.3390/mi8010023.
[17] M.C.H. Karg, A. Munk, B. Ahuj, M. Veit Backer, J.P. Schmitt, C. Stengel, S. Vyacheslavovich Kuryntsev, M. Schmidt, Expanding particle size distribution and morphology of aluminium-silicon powders for laser beam melting by dry coating with silica nanoparticles, J. Mater. Process. Technol. 264 (2019) 155–171.
[18] A. Fabrizi, S. Capuzzi, A. De Mori, G. Timelli, Effect of T6 heat treatment on the microstructure and hardness of secondary AlSi9Cu3(Fe) alloys produced by semi-solid SEED process, Metals (Basel) 8 (2018) https://doi.org/10.3390/met8100750.
[19] M. Starink, The determination of activation energy from linear heating rate experiments: a comparison of the accuracy of isoconversion methods, Thermochim. Acta 404 (2003) 163–176, https://doi.org/10.1016/S0040-6031(03)00144-8.
[20] M.J. Starink, On the applicability of isoconversion methods for obtaining the activation energy of reactions within a temperature-dependent equilibrium state, J. Mater. Sci. 32 (1997) 6505–6512, https://doi.org/10.1023/A:1018655026036.
[21] J. Farjas, P. Roura, Modification of the Kolmogorov-Johnson-Mehl-Avrami rate equation for non-isothermal experiments and its analytical solution, Acta Mater. 54 (2006) 5573–5579, https://doi.org/10.1016/j.actamat.2006.07.037.
[22] M.J. Starink, Activation energy determination for linear heating experiments: deviations due to neglecting the low temperature end of the temperature integral, J. Mater. Sci. 42 (2007) 483–489, https://doi.org/10.1007/s10853-006-1067-7.
[23] E.O. Olakanmi, R.F. Cochrane, K.W. Dalgarno, A review on selective laser sintering/melting (SLS/SLM) of aluminium alloy powders: processing, microstructure, and

properties, J. Prog. Mater. Sci. 74 (2015) 401–477, https://doi.org/10.1016/j.pmatsci.
2015.03.002.

[24] J. Fiocchi, A. Tuissi, P. Bassani, C.A. Biffi, Low temperature annealing dedicated to
AlSi10Mg selective laser melting products, J. Alloys Compd. 695 (2017)
3402–3409, https://doi.org/10.1016/j.jallcom.2016.12.019.

[25] A. Rodríguez-Veiga, B. Bellón, I. Papadimitriou, G. Esteban-Manzanares, I. Sabirov, J.
LLorca, A multidisciplinary approach to study precipitation kinetics and hardening
in an Al-4Cu (wt.%) alloy, J. Alloys Compd. 757 (2018) 504–519, https://doi.org/
10.1016/j.jallcom.2018.04.284.

[26] D. Ovono, I. Guillot, D. Massinon, Determination of the activation energy in a cast al-
uminium alloy by TEM and DSC, J. Alloys Compd. 432 (2007) 241–246, https://doi.
org/10.1016/j.jallcom.2006.05.132.

[27] M. Fatmi, B. Ghebouli, M.A. Ghebouli, T. Chihi, M.A. Hafiz, The kinetics of precipita-
tion in Al-2.4wt% Cu alloy by Kissinger, Ozawa, Bosswel and Matusita methods,
Phys. B 406 (2011) 2277–2280, https://doi.org/10.1016/j.physb.2011.03.053.

[28] P. Heugue, D. Larouche, F. Breton, R. Martinez, X.G. Chen, Evaluation of the growth
kinetics of θ' and θ-Al2Cu precipitates in a binary Al-3.5 Wt Pct cu alloy, Metall.
Mater. Trans. A. (2019) https://doi.org/10.1007/s11661-019-05227-8.

[29] L.M. Rylands, D.M.J. Wilkes, W.M. Rainforth, H. Jones, Coarsening of precipitates and
dispersoids in aluminium alloy matrices: a consolidation of the available experi-
mental data, J. Mater. Sci. 29 (1994) 1895–1900.

[30] Y. Adda, J. Philibert, La diffusion dans les solides, 2, 1966 Paris.

[31] I.S. Grigoriev, E.Z. Meĭlikhov, A.A. Radzig, Handbook of Physical Quantities, CRC,
1997.

[32] S. Fu, D. Yi, H. Liu, Y. Jiang, B. Wang, Z. Hu, Effects of external stress aging on mor-
phology and precipitation behavior of θ" phase in Al—Cu alloy, Trans. Nonferrous
Met. Soc. China. 24 (2014) 2282–2288, https://doi.org/10.1016/S1003-6326(14)
63345-8.

[33] C. Colombo, C.A. Biffi, J. Fiocchi, A. Tuissi, L.M. Vergani, Effect of optimized heat treat-
ments on the tensile behavior and residual stresses of selective laser melted
AlSi10Mg samples, Key Eng. Mater. 813 (2019) 364–369, https://doi.org/10.4028/
www.scientific.net/KEM.813.364.

[34] E.M. Elgallad, Z. Zhang, X.G. Chen, Effect of quenching rate on precipitation kinetics
in AA2219 DC cast alloy, Phys. B Condens. Matter 514 (2017) 70–77, https://doi.org/
10.1016/j.physb.2017.03.039.

[35] H. Liu, B. Bellón, J. LLorca, Multiscale modelling of the morphology and spatial distri-
bution of θ' precipitates in Al-Cu alloys, Acta Mater. 132 (2017) 611–626, https://
doi.org/10.1016/j.actamat.2017.04.042.

[36] E.M. Elgallad, Z. Zhang, X.G. Chen, Effect of two-step aging on the mechanical prop-
erties of AA2219 DC cast alloy, Mater. Sci. Eng. A 625 (2015) 213–220, https://doi.
org/10.1016/j.msea.2014.12.002.

[37] X. Wang, L.N. Carter, B. Pang, M.M. Attallah, M.H. Loretto, Microstructure and yield
strength of SLM-fabricated CM247LC Ni-Superalloy, Acta Mater. 128 (2017)
87–95, https://doi.org/10.1016/j.actamat.2017.02.007.

[38] L. Liu, Q. Ding, Y. Zhong, J. Zou, J. Wu, Y. Chiu, J. Li, Z. Zhang, Q. Yu, Z. Shen, Disloca-
tion network in additive manufactured steel breaks strength – ductility trade-off,
Mater. Today 21 (2018) 354–361, https://doi.org/10.1016/j.mattod.2017.11.004.

[39] J. Wu, X.Q. Wang, W. Wang, M.M. Attallah, M.H. Loretto, Microstructure and
strength of selectively laser melted AlSi10Mg, Acta Mater. 117 (2016) 311–320,
https://doi.org/10.1016/j.actamat.2016.07.012.

[40] C.A. Biffi, J. Fiocchi, A. Tuissi, Selective laser melting of AlSi10 Mg: influence of pro-
cess parameters on Mg2Si precipitation and Si spheroidization, J. Alloys Compd.
755 (2018) 100–107, https://doi.org/10.1016/j.jallcom.2018.04.298.

[41] S.I. Fujikawa, K.I. Hirano, Y. Fukushima, Diffusion of silicon in aluminum, Metall.
Trans. A. 9 (1978) 1811–1815, https://doi.org/10.1007/BF02663412.

[42] S.K. Pabi, On the dissolution kinetics of silicon in an aluminum-rich alloy, Mater. Sci.
Eng. 43 (1980) 151–158.

[43] R.S. Yassar, D.P. Field, H. Weiland, The effect of cold deformation on the kinetics of
the beta" precipitates in an Al-Mg-Si alloy, Metall. Mater. Trans. A. 36 (2005)
2059–2065.

[44] Q. Jia, P. Rometsch, P. Kürnsteiner, Q. Chao, A. Huang, M. Weyland, L. Bourgeois, X.
Wu, Selective laser melting of a high strength Al-Mn-Sc alloy: alloy design and
strengthening mechanisms, Acta Mater. 171 (2019) 108–118, https://doi.org/10.
1016/j.actamat.2019.04.014.

[45] B. Chen, S.K. Moon, X. Yao, G. Bi, J. Shen, J. Umeda, K. Kondoh, Strength and strain
hardening of a selective laser melted AlSi10Mg alloy, Scr. Mater. 141 (2017)
45–49, https://doi.org/10.1016/j.scriptamat.2017.07.025.

[46] K.V. Yang, P. Rometsch, C.H.J. Davies, A. Huang, X. Wu, Effect of heat treatment on
the microstructure and anisotropy in mechanical properties of A357 alloy produced
by selective laser melting, Mater. Des. 154 (2018) 275–290, https://doi.org/10.1016/
j.matdes.2018.05.026.

[47] https://www.slm-solutions.com/fileadmin/user_upload/MDS_AL-Alloy_AlSi9Cu3_
0219.pdf.

[48] J. Fiocchi, C.A. Biffi, C. Colombo, L.M. Vergani, A. Tuissi, Ad hoc heat treatments for
selective laser melted AlSi10mg alloy aimed at stress-relieving and enhancing me-
chanical performances, J. Mater. (2020) https://doi.org/10.1007/s11837-019-
03973-z.

[49] A. Salmi, E. Atzeni, History of residual stresses during the production phases of
AlSi10Mg parts processed by powder bed additive manufacturing technology, Vir-
tual Phys. Prototyp. 12 (2017) 153–160, https://doi.org/10.1080/17452759.2017.
1310439.

[50] D.R. Manca, A.Y. Churyumov, A.V. Pozdniakov, A.S. Prosviryakov, D.K. Ryabov, A.Y.
Krokhin, V.A. Korolev, D.K. Daubarayte, Microstructure and properties of novel
heat resistant Al–Ce–Cu alloy for additive manufacturing, Met. Mater. Int. 25
(2019) 633–640, https://doi.org/10.1007/s12540-018-00211-0.

[51] L. Zhuo, Z. Wang, H. Zhang, E. Yin, Y. Wang, T. Xu, C. Li, Effect of post-process heat
treatment on microstructure and properties of selective laser melted AlSi10Mg
alloy, Mater. Lett. 234 (2019) 196–200, https://doi.org/10.1016/j.matlet.2018.09.
109.

[52] K.G. Prashanth, Work hardening in selective laser melted Al-12Si alloy, Mater. Des.
Process Commun. 1 (2019) 10–13, https://doi.org/10.1002/mdp2.46.

[53] L.A. Dobrzañski, R. Maniara, J.H. Sokolowski, The effect of cooling rate on microstruc-
ture and mechanical properties of AC AlSi9Cu alloy, Analysis 28 (2007) 105–112.

[54] M. Panušková, E. Tillovà, M. Chalupovà, Relation between mechanical properties
and microstructure of cast aluminum alloy AlSi9Cu3, Strength Mater 40 (2008)
109–112.

[55] M. Zamani, S. Seifeddine, A.E.W. Jarfors, High temperature tensile deformation be-
havior and failure mechanisms of an Al–Si–Cu–Mg cast alloy — the microstructural
scale effect, Mater. Des. 86 (2015) 361–370, https://doi.org/10.1016/j.matdes.2015.
07.084.

[56] M. Vončina, N. Močnik, A. Nagode, A. Stoić, M. Bizjak, Dependence of mechanical
properties on Cu content in AlSi9Cu3(Fe) alloy, Teh. Vjesn. 24 (2017) 229–231,
https://doi.org/10.17559/TV.